

## Diagnostic Complex of the Globus-M2 Spherical Tokamak

Yu. V. Petrov<sup>a,\*</sup>, P. A. Bagryansky<sup>b</sup>, I. M. Balachenkov<sup>a</sup>, N. N. Bakharev<sup>a</sup>, P. N. Brunkov<sup>a</sup>,  
V. I. Varfolomeev<sup>a</sup>, A. V. Voronin<sup>a</sup>, V. K. Gusev<sup>a</sup>, V. A. Goryainov<sup>a</sup>, V. V. Dyachenko<sup>a</sup>,  
N. V. Ermakov<sup>a</sup>, E. G. Zhilin<sup>d</sup>, N. S. Zhiltsov<sup>a</sup>, S. V. Ivanenko<sup>b</sup>, M. V. Il'yasova<sup>a</sup>, A. A. Kavinc,  
E. O. Kiselev<sup>a</sup>, A. N. Kononov<sup>a</sup>, S. V. Krikunov<sup>a</sup>, G. S. Kurskiev<sup>a</sup>, A. D. Melnik<sup>a</sup>, V. B. Minaev<sup>a</sup>,  
A. B. Mineev<sup>c</sup>, I. V. Miroshnikov<sup>a</sup>, E. E. Mukhin<sup>a</sup>, A. N. Novokhatsky<sup>a</sup>, A. V. Petrov<sup>e</sup>,  
A. M. Ponomarenko<sup>e</sup>, N. V. Sakharov<sup>a</sup>, O. M. Skrekel<sup>a</sup>, A. E. Solomakhin<sup>b</sup>, V. V. Solokha<sup>a</sup>,  
A. Yu. Telnova<sup>a</sup>, E. E. Tkachenko<sup>a</sup>, V. A. Tokarev<sup>a</sup>, S. Yu. Tolstyakov<sup>a</sup>, E. A. Tukhmeneva<sup>a</sup>,  
E. M. Khil'kevich<sup>a</sup>, N. A. Khromov<sup>a</sup>, F. V. Chernyshev<sup>a</sup>, A. E. Shevelev<sup>a</sup>,  
P. B. Shchegolev<sup>a</sup>, K. D. Shulyat'ev<sup>a</sup>, and A. Yu. Yashin<sup>a,e</sup>

<sup>a</sup>*Ioffe Institute, Russian Academy of Sciences, St. Petersburg, 194064 Russia*

<sup>b</sup>*Budker Institute of Nuclear Physics, Siberian Branch, Russian Academy of Sciences, Novosibirsk, 630090 Russia*

<sup>c</sup>*Efremov Institute of Electrophysical Apparatus, St. Petersburg, 196641 Russia*

<sup>d</sup>*"Ioffe Fusion Technology," St. Petersburg, 194021 Russia*

<sup>e</sup>*Peter the Great St. Petersburg Polytechnic University, St. Petersburg, 195251 Russia*

\**e-mail: yu.petrov@mail.ioffe.ru*

Received June 29, 2023; revised September 10, 2023; accepted September 25, 2023

**Abstract**—The diagnostic complex of the Globus-M2 spherical tokamak ( $R = 36$  cm,  $a = 24$  cm), the only operating tokamak in Russia with a divertor plasma configuration, which operates in the range of subthermo-nuclear temperatures ( $T_e$  to 1.6 keV,  $T_i$  to 4.5 keV) and densities ( $n_e$  to  $2 \times 10^{20}$  m<sup>-3</sup>), is described. The Globus-M2 tokamak is the unique scientific facility, which is a part of the Federal Center for Collective Use of the Ioffe Institute, Russian Academy of Sciences “Materials Science and Diagnostics in Advanced Technologies.” This allows third parties to perform their research using it. The work contains a list of all diagnostics currently available on the tokamak. The description of the diagnostics is structured in such a way that the reader gets an idea of their capabilities for measuring plasma parameters with an emphasis on the limits and accuracy of the measured values, and also spatial and time resolution. At the same time, many technical details are omitted in order to save space; references are given to papers with a more detailed description of individual diagnostics.

**Keywords:** spherical tokamak, high-temperature plasma diagnostics

**DOI:** 10.1134/S1063780X23601360

### 1. INTRODUCTION

The modernized Globus-M2 spherical tokamak (major radius  $R = 36$  cm, minor radius  $a = 24$  cm) [1] was launched in 2018. As a result of the modernization of the electromagnetic system, the design parameters of the tokamak were significantly increased: the toroidal magnetic field  $B_T$  to 1 T and plasma current  $I_p$  to 500 kA. Currently, the discharges have been obtained at the tokamak at  $B_T = 0.9$  T and  $I_p = 450$  kA. As a result of increasing the current and field, the plasma parameters increased significantly. In experiments with additional plasma heating by high-energy atomic beams, the central ion temperature  $T_i(0)$  reached 4.5 keV at the central electron temperature  $T_e(0)$  of higher than 1.5 keV [2]. In addition to neutral atom injectors, the tokamak is equipped with ion cyclotron

heating (ICH) [3] and lower hybrid current generation complexes [4]. Globus-M2 is the only spherical tokamak in the world that uses these RF systems. It is also the only operating tokamak in Russia with a divertor plasma configuration, operating in modes with lower, upper or two X-points. The tokamak has an extensive set of diagnostics. The list of diagnostics is given in Table 1, and their location in the tokamak is given in Fig. 1. All of the above allows the performance of research on a wide range of topics on the Globus-M2 tokamak. The Globus-M2 tokamak is the unique scientific facility, which is a part of the Federal Center for Collective Use of the Ioffe Institute, Russian Academy of Sciences “Materials Science and Diagnostics in Advanced Technologies.” This allows third-party organizations to conduct their research on it. Recently, this is implemented on an increasingly large

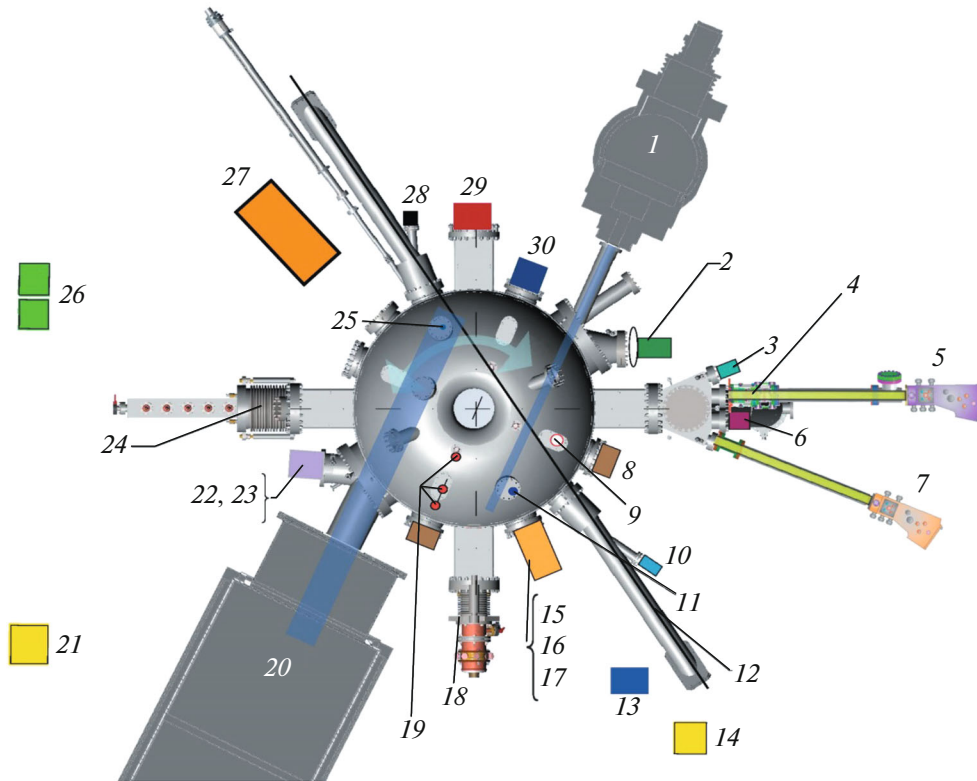


**Fig. 1.** Location of diagnostics at the Globus-M2 tokamak: (1) injector of atoms with the particle energy of 18–40 keV; (2) collecting system for the Thomson scattering diagnostics; (3) diagnostics of radiation losses; (4) foil soft X-ray detector; (5) AKORD-12 neutral particle analyzer; (6)  $D\alpha$  sensor; (7) AKORD-24M neutral particle analyzer; (8) camera obscura of soft X-ray radiation; (9) divertor Thomson scattering diagnostics; (10) laser interferometer; (11) thermal imager; (12) probing laser for the Thomson scattering diagnostics; (13)  $^3\text{He}$  neutron counters; (14)  $^{10}\text{B}$  neutron counter (movable); (15) plasma gun; (16) movable Langmuir probe; (17) compact neutral particle analyzer (CNPA); (18) ICR antenna; (19) microwave interferometer; (20) injector of atoms with the particle energy of 30–50 keV; (21)  $^{10}\text{B}$  neutron counter (in protection); (22) helium thermometer; (23) video camera; (24) grill antenna for lower hybrid current generation; (25) soft X-ray radiation detector; (26)  $\text{LaBr}_3(\text{Ce})$  hard X-ray spectrometer; (27) BC-501A neutron spectrometer; (28) diagnostics of effective plasma charge; (29) multichannel Doppler reflectometer; (30) diagnostics of charge exchange spectroscopy.

scale. In this regard, there is a need to demonstrate the experimental capabilities of the facility to the scientific community. In agreement with the editors of the journal “Plasma Physics,” it was decided to devote its special issue to research carried out on the Globus-M2 tokamak, which, in particular, includes works describing the tokamak itself and its heating complex. This work is devoted to the description of the tokamak diagnostic complex. The description of the diagnostics is structured in such a way that the reader gets an idea of their capabilities for measuring plasma parameters with an emphasis on the limits and accuracy of the measured values, and also spatial and time resolution. At the same time, many technical details are omitted in order to save space; references are given to papers presenting a more detailed description of individual diagnostics.

## 2. MAGNETIC DIAGNOSTICS

### 2.1. Magnetic Loops

To obtain information about the poloidal magnetic flux and its distribution, 21 full-circuit toroidal loops are used. The loops are made of kirsicable, in which the central nichrome wire is protected through insulation by a stainless steel tube with a diameter of 1.5 mm. Seven loops are laid along the inner surface of the vacuum vessel, and fourteen are located outside (their location, as well as the location of the poloidal coils, is shown in Fig. 2). Signals from the loops, along with signals from the Rogowski coils, which measure currents in the poloidal coils and current in the plasma, are recorded during the discharge using an ADC. Subsequently, these data are used to restore equilibrium using three different codes: pyGSS [5], PET [6] and the movable current ring method [7]. A mathematical model of the tokamak was derived for the operation of these three codes. The model includes all coils that

**Table 1.** List of diagnostics for the Globus-M2 tokamak

Purpose	Name	Characteristics
<b>Magnetic measurements</b>		
Plasma current	Rogowski coils	2 coils inside the vessel
Bypass voltage	Loops	2 toroidal loops
Plasma energy content	Diamagnetic loops	2 poloidal loops
Plasma position and shape	Loops	2 saddle and 24 toroidal loops
MHD plasma perturbations	Magnetic probes	2 poloidal arrays of 28 and 15 probes each and 1 toroidal array of 8 probes Three-coordinate probe
<b>Kinetic measurements</b>		
$T_e$ and $n_e$ profiles	Thomson scattering, main array Thomson scattering in the divertor region Movable Langmuir probe	Profiles over 11 spatial points in the equatorial plane with an interval of 3 ms, the entire discharge Measurements in 9 spatial points, with an interval of 10 ms $T_e$ , $n_e$ profiles behind the separatrix
Integral chord density $n_e L$	Microwave interferometer Laser interferometer	$\lambda = 1$ mm, 3 vertical chords $\lambda = 9.6$ $\mu$ m, 1 horizontal chord
$T_i$ profiles of the plasma toroidal rotation velocity	Active charge exchange spectroscopy (CXRS) diagnostics	8 spatial points over the major radius with an interval of 5 ms
<b>Spectroscopy</b>		
$Z_{\text{eff}}$ measurement	Filter monochromator	Measurements of continuum in ranges of $\lambda = 1019$ – $1040$ and $\lambda = 948$ – $952$ nm
Control of input of impurities into plasma	Overview Avantes AvaSpec-ULS2048 spectrometer filter spectrometer	Emission of impurity lines in the range $\lambda = 200$ – $1100$ nm CIII, OII, FeI, NII, BII, HeI lines in the monitor mode
Working gas flow control	Filter monochromators	D $\alpha$ radiation from the region of the upper and lower X-point and along two vertical chords
Radiation losses	SPD photodiodes	Measurements of radiation in a wide spectral range $\lambda = 200$ – $1100$ nm along central and peripheral chords
Soft X-ray radiation (SXR)	Camera obscura with a line of 16 photodiodes four-foil SXR spectrometer	Measurement SXR through 50 $\mu$ m beryllium filter in the poloidal section monitor estimate $T_e(0)$
<b>Corpuscular measurements</b>		
Temperature and ion distribution function	Neutral particle analyzers (NPA and CNPA)	AKORD-12, transverse orientation, horizontal and vertical scanning, AKORD-24M and CNPA, longitudinal orientation, horizontal scanning
Hard X-ray radiation (HXR)	Gamma-spectrometers on LaBr <sub>3</sub> (Ce) crystals HXR detector on the NaI(Tl) crystal	Two spectrometers, measurement range 0.2–20 MeV monitor measurements of the HXR flux
Neutron radiation	BC-501A liquid scintillator spectrometers SNM-11 corona counters He <sup>3</sup> proportional counters	Two spectrometers with a neutron energy range of 0.1–5 MeV monitor measurements of neutron fluxes

Table 1. (Contd.)

Purpose	Name	Characteristics
<b>Heat fluxes to the wall</b>		
Wall temperature	Thermal imager Two-color pyrometer Langmuir diver- tor probes	Temperature measurements of divertor plates in the range of 5–1500°C, with frequency up to 1.5 kHz measurements of the wall temperature in the range of 70–3500°C measurement of heat fluxes to the divertor plates
<b>Video observations</b>	Video cameras Olympus i-SPEED 2 Optronis CamRecord CR3000x2	Video observation of plasma processes, including fast ones, at speeds up to 100000 frames/s
<b>Reflectometry</b>	Doppler reflectometer	Measurement of the radial profile of the plasma rotation speed in the direc- tion $\mathbf{E} \times \mathbf{B}$ turbulence study

produce an external magnetic field, and also the vacuum vessel.

The current ring method is used to calculate the plasma boundary between discharges owing to its simplicity and high operation speed. Such results are

achieved by greatly simplifying the plasma model and refusing to solve the Grad–Shafranov equation. In the current ring method, the plasma current is simulated by a set of movable current rings. Their position and current are adjusted to the measured plasma current and to the measurements of the poloidal magnetic flux using magnetic loops. The disadvantages of the method include the impossibility of determining the distribution of equilibrium plasma pressure, toroidal current density, etc. Therefore, a module was written for it that makes it possible to determine the stored energy of the plasma, poloidal and toroidal beta, and also the internal inductance of the plasma using the method of Shafranov integrals [8]. The other two codes require more labor-intensive processing by solving the Grad–Shafranov equation, but as a result, they calculate all the necessary geometric and integral parameters, such as the minor and major radii of the plasma and the position of the magnetic axis, the position of the X-point, poloidal beta, internal inductance, diamagnetic flux, and stored energy. The result of all three codes in the form of the plasma boundary and poloidal magnetic field flux from pyGSS for the discharge no. 42368,  $t = 200$  ms ( $I_p = 400$  kA,  $B_T = 0.8$  T), together with the magnetic system are shown in Fig. 2. In the PET code, the diamagnetic flux is used as an additional fitting parameter, which is measured using a loop encircling the vacuum vessel along a poloidal bypass. The flux of the vacuum toroidal magnetic field is compensated using a Rogowski coil, which measures the current in the toroidal coil. At the same time, the reliability of calculations of the magnetic configuration and calculated integral plasma parameters increases.

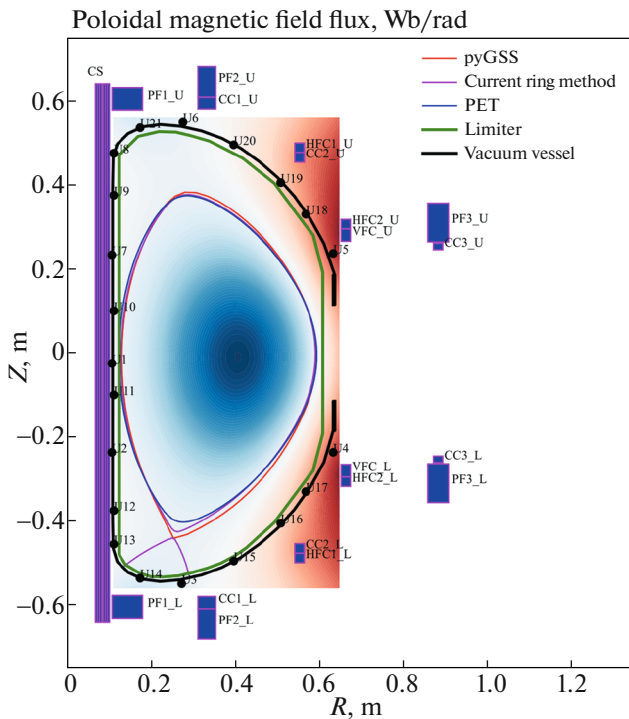
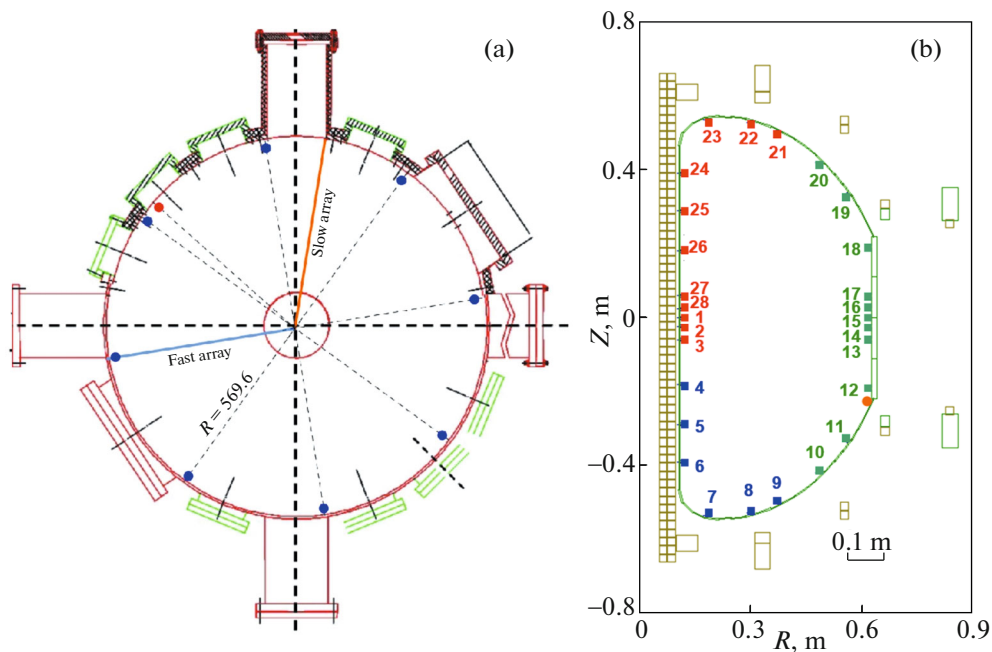


Fig. 2. Location of poloidal coils, measuring magnetic loops and reconstruction results of the magnetic surface shape using pyGSS, PET codes, and the current ring method for the discharge no. 42368,  $t = 200$  ms,  $I_p = 400$  kA,  $B_T = 0.8$  T.



**Fig. 3.** Location of magnetic probes at the Globus-M2 facility: toroidal array and three-coordinate probe (red) (a); low-frequency poloidal array (b). Orange indicates the position of the toroidal arrays in the poloidal cross section in (a), and the position of the poloidal arrays in the toroidal section in (b). Light blue indicates the position of high-frequency poloidal arrays.

## 2.2. Magnetic Probes

The magnetic probe diagnostics at the Globus-M2 tokamak is represented by a toroidal array of probes, two poloidal arrays, and also a three-coordinate probe for measuring the polarization of magnetic disturbances.

The toroidal array is mounted inside the lower toroidal diaphragm of the tokamak ( $R = 57$  cm,  $Z = -23$  cm) and consists of 8 probes evenly spaced along the toroidal bypass oriented towards the vertical component of the magnetic field (Fig. 3a). The probes are coils of copper wire in polyimide insulation, wound on a ceramic mandrel, located inside a vacuum vessel and protected from heat and particle fluxes only by graphite plates. High-frequency electromagnetic radiation can penetrate into the region where probes are mounted through the gaps between the plates. The design of the probes in combination with a fast ADC makes it possible to measure signals with frequencies up to hundreds of MHz.

The poloidal array (Fig. 3b) is designed to record slow MHD oscillations and consists of 28 cylindrical coils mounted inside thin-walled stainless steel tubes with a wall thickness of 0.5 mm, which prevents the passage of electromagnetic waves with frequencies above 150 kHz. Recently, another poloidal array of 16 probes with frequency characteristics similar to those of the toroidal array was mounted in the tokamak, but the acquisition of a fast ADC for it is still only in the plans. Also there is a three-coordinate probe at

the tokamak, which consists of three separate magnetic coils, similar to the probes of a toroidal array designed to determine the polarization of magnetic disturbances.

The magnetic diagnostics of the Globus-M tokamak makes it possible to record electromagnetic radiation in a wide frequency range and study the structure of various MHD instabilities, such as tearing modes in the range of 5–20 kHz [9], shear Alfvén modes [10] in the range of 50–500 kHz, compression Alfvén modes with frequencies on the order of 1 MHz [11], ion cyclotron radiation (5–20 MHz), and also higher frequency oscillations at helicon frequencies. As an example, Fig. 4 shows a spectrogram of signals from a toroidal array of probes for toroidal Alfvén modes in the discharge no. 42655. The toroidal mode wavenumbers (highlighted in color) are determined using the spatial Fourier transform.

## 3. THOMSON SCATTERING DIAGNOSTICS

The Thomson scattering (TS) diagnostics at the Globus-M2 tokamak consists of two complexes. The first was significantly updated in 2020 and provides the measurements of temperature and electron density profiles in the equatorial plane [12]. Plasma probing is carried out using a 1064.5-nm Nd:YAG laser with a pulse duration of  $\sim 10$  ns significantly shorter than the characteristic times of the MHD plasma activity, i.e., the TS diagnostic measurements can be considered instantaneous. Laser radiation from 11 spatial points

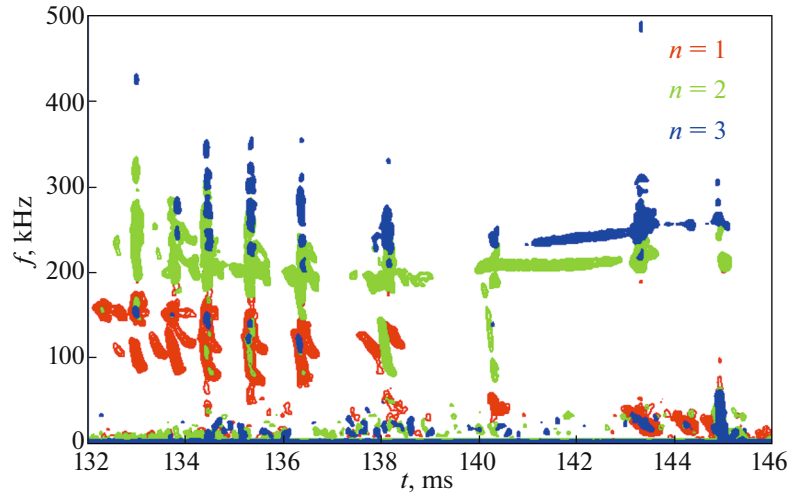


**Fig. 4.** Determination of mode numbers from signals of the array of toroidal probes using spatial Fourier transform. Discharge no. 43338.

of intersection of the probe laser beam and observation chords scattered on the plasma is collected by the receiving lens (Fig. 5). In a laser pulse, spatial temperature  $T_e(R)$  and electron density  $n_e(R)$  profiles are

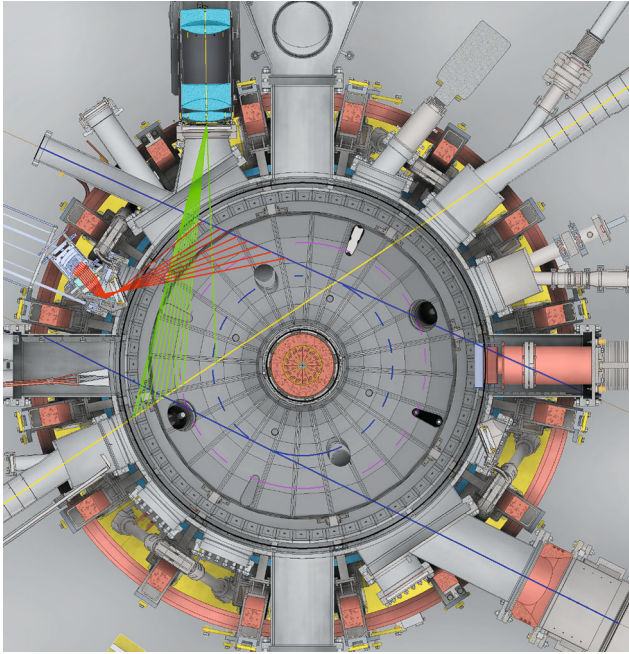


**Fig. 5.** Diagram of the geometry of TS and CRXS diagnostic measurements in the equatorial cross section of the Globus-M2 tokamak. Black circles indicate the position of the plasma-facing graphite surface. The dashed purple line shows the magnetic axis of the plasma. Green crosses indicate TS diagnostic measurement points on the probing chord (yellow line). Red crosses indicate CRXS diagnostic measurement points on the NBII heating beam (blue line).

measured. The probing laser operates with a pulse repetition rate of 330 Hz, providing the measurement of the dynamics  $T_e(R, t)$  and  $n_e(R, t)$  with a step of 3.03 ms during the total discharge of the tokamak. The spatial resolution is in the range from 11 mm on the high-field side (HFS) ( $R = 23$  cm,  $r/a = -0.5$ ) to 21 mm on the low-field side (LFS) ( $R = 57$  cm,  $r/a = 0.9$ ) and 10 mm for two extreme points on the low-field side ( $R = 60$  cm,  $r/a = 1$ ). The observation region includes the space from the LFS of the separatrix to the magnetic axis of the plasma, plus one point on the HFS. TS diagnostic data is available in real time with a delay of  $< 2.4$  ms; data verified by the diagnostic operator enters the database during the pause between tokamak discharges.

The diagnostics provides the measurement of  $T_e(R, t)$  in the range from 6 to 5 keV and  $n_e(R, t)$  in the range from  $5 \times 10^{17}$  to  $3 \times 10^{20} \text{ m}^{-3}$ . Information on the temperature and electron density distribution makes it possible to calculate the electron pressure profile  $P_e(R, t)$ . The position of the magnetic axis is estimated from the position of the  $P_e(R)$  maximum. The analysis of the shape of the  $T_e(R, t)$  and  $n_e(R, t)$  profiles makes it possible to localize MHD instabilities such as magnetic islands. The inversion radius  $R_{\text{inv}}$  is determined for sawtooth oscillations. Figure 6 shows a typical example of measuring the electron temperature in the sawtooth mode. It is possible to carry out measurements beyond the last closed magnetic surface (LCFS) because of the high diagnostic sensitivity, which makes it possible to determine the LCFS position in the equatorial plane  $R_{\text{sep}}$ . Given data on the magnetic configuration, the profiles measured by the TS diagnostic can be projected onto the full poloidal cross section [13], obtaining  $T_e(R, Z, t)$  and  $n_e(R, Z, t)$  under the assumption of the conservation of the kinetic param-

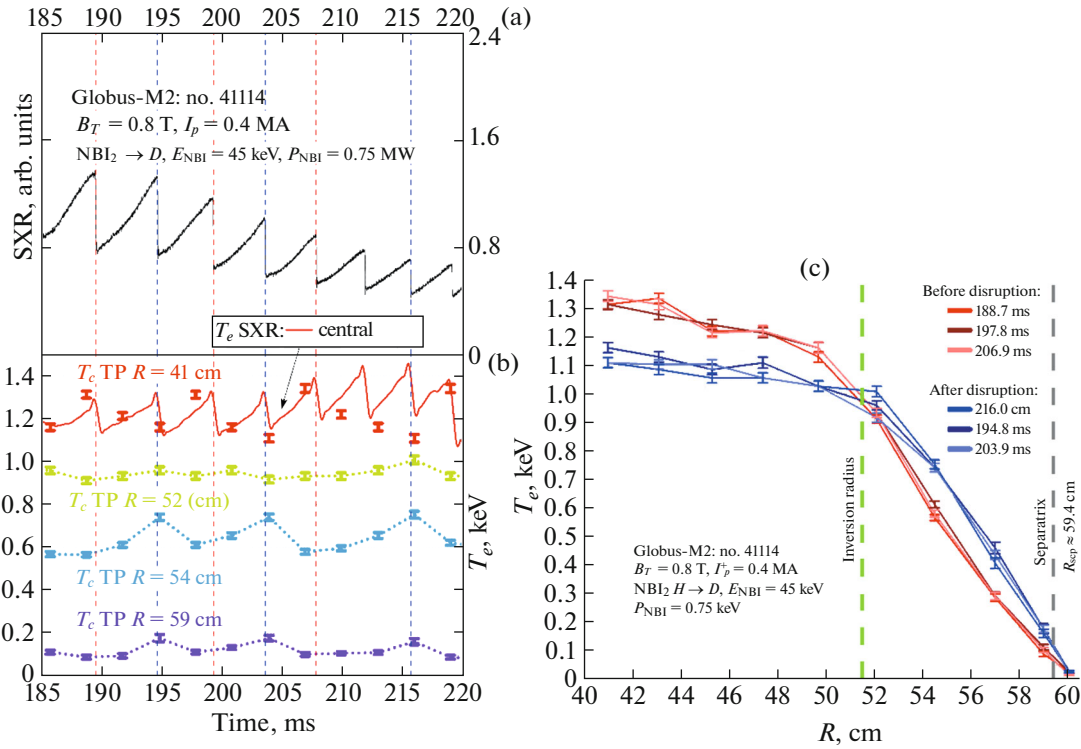


**Fig. 6.** Oscillogram of the soft X-ray radiation signal shows sawtooth oscillations in the Globus-M2 discharge no. 41114 with additional heating by neutral injection; moments of disruption of sawtooth oscillations are highlighted by vertical dotted lines (a). Dynamics of electron temperature during sawtooth oscillations (b). The solid red line shows the estimate of the central temperature according to the foil soft X-ray radiation spectrometer. The dots show temperature measurements using Thomson scattering diagnostics in the following regions along the major radius: (red) 41 cm (central), (green) 52 cm, (blue) 54 cm, and (violet) 59 cm. Electron temperature profiles from Thomson scattering diagnostics measured before sawtooth relaxation (red) and after (blue) (c). The legend shows the times at which the measurement was carried out. The green dashed line shows the inversion radius.

ters of electrons within a magnetic surface. Diagnostic capabilities are described in [14] in more detail.

The TS diagnostic data is consistent with a number of independent tokamak diagnostics. Absolute measurements of  $n_e$  are verified by data from a dispersive laser interferometer and microwave interferometer. The position of the magnetic axis and  $R_{inv}$  is compared with the magnetic equilibrium reconstruction. The  $R_{sep}$  position and the  $T_e(R, t)$  value in the vicinity of the separatrix can be compared with probe measurements. The integral  $W_e(t)$  value is compared with the estimate from diamagnetic measurements and simulation by equilibrium codes, pyGSS [5] and PET [6].

The second TS diagnostic complex is located in the region where the separatrix exits the lower dome of the vessel (Fig. 7). The purpose of this system is to carry out local measurements of the electron temperature  $T_e(z, t)$  in the range of 1–100 eV and density  $n_e(z, t)$  in the range of  $10^{17}$ – $10^{20}$   $m^{-3}$ . The source of probing radiation is a Nd:YAG laser generating pulses with a duration of 3 ns, an energy of 2 J, and a frequency of 100 Hz at a wavelength of 1064 nm. The short duration of the laser pulse (noticeably shorter than the charac-

teristic MHD times) provides the high time resolution and also minimizes the effect of background plasma radiation on measurements. The diagnostic complex is aimed at providing real-time data with a delay of no more than 3 ms. Scattered radiation is collected from 9 spatial points along a vertical probing chord 110 mm long, which passes at a radius  $R = 24$  cm. Depending on the magnetic configuration, it is possible to study the region under the X-point bounded by the inner and outer branches of the separatrix (private flux region), the plasma in the vicinity of the X-point or the edge plasma on the inner bypass. A more detailed description of the diagnostics is given in [15].

Currently the diagnostics is in the debugging stage. The first diagnostic results were obtained in the summer campaign of 2022. The measurements were carried out at one spatial point. The magnetic configuration shifted with respect to the measurement point in the stationary phase of the discharge, which made it possible to obtain a temperature profile in the region of the inner leg of the separatrix. Figure 8 shows magnetic configurations at various times and the location of the measurement point with respect to them.

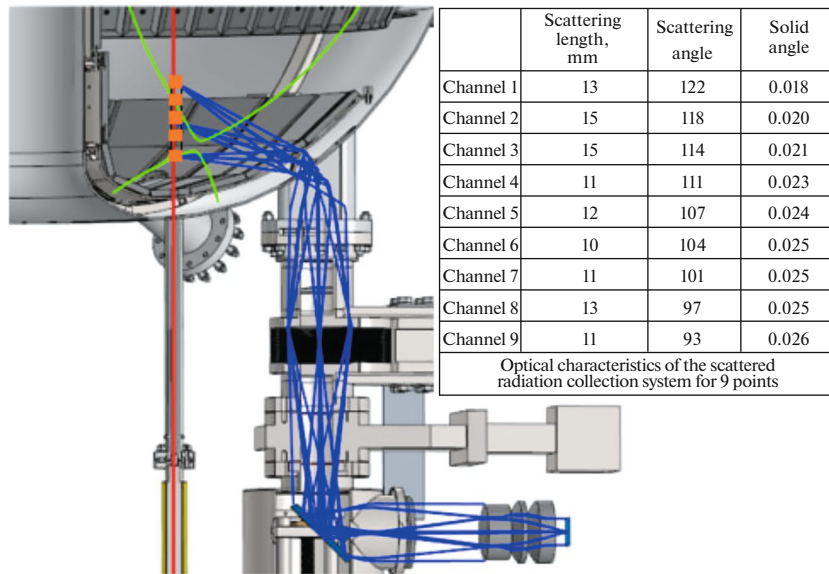


**Fig. 7.** Scheme of radiation collection by TS diagnostics in the divertor region of the Globus-M2 tokamak. Red color indicates the probing chord, green color indicates the magnetic configuration of the plasma, and blue color indicates the path of rays in the light collection system.

To measure ultra-low  $T_e$  values, two spectral channels closest to the laser wavelength were added. A spectral channel less than 1 nm wide in the short-wavelength part of the spectrum is formed by mounting sequentially two filters from the same batch, but with a scatter of spectral characteristics during manufacturing.

#### 4. NEUTRAL PARTICLE ANALYZERS

The Globus-M2 tokamak uses three neutral particle analyzers: two AKORD-type analyzers [16]

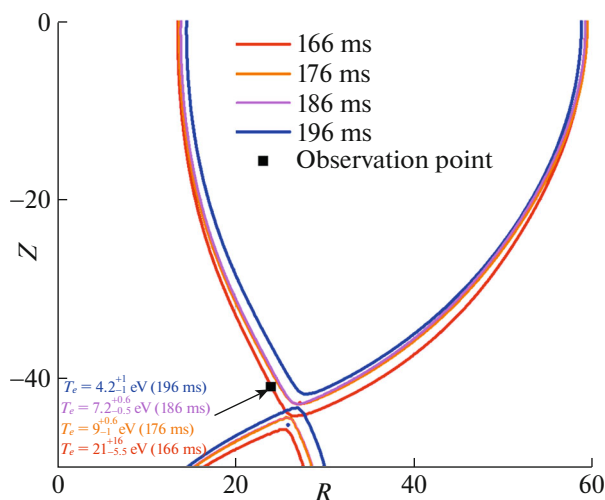


**Fig. 8.** Results of  $T_e$  measurements in the region of the inner leg of the separatrix.

(AKORD-24M and AKORD-12) and a compact CNPA-09 analyzer [17]. Analyzers are used to determine the ion temperature, plasma isotopic composition, and also to record the spectrum of high-energy ions that arise when using additional heating methods. The location of the analyzers is shown in Fig. 1, and their main characteristics are given in Table 2.

The physical basis of measurements using neutral particle analyzers at the Globus-M2 tokamak, and also the main results obtained using this diagnostic, are described in [18]. The analyzers can operate in the passive mode, when the signal is integrated along the entire diagnostic observation line, and in the active mode [19, 20], when the main signal source is formed in the intersection region of the beam of injected high-energy atoms and the analyzer observation line. The use of the active diagnostic mode makes it possible to localize the measurements, which greatly simplifies the interpretation of experimental results. The AKORD-24M and AKORD-12 analyzers use the injector 1 for active measurements; in the near future, a CNPA-09 analyzer will be mounted in a new position, in which the injector 2 will be used for active measurements. The AKORD-type analyzers are equipped with a spatial scanning system that makes it possible to change the observation line from discharge to discharge. Scanning systems allow vertical scanning at  $\pm 10^\circ$  with respect to the equatorial plane, and also horizontal scanning for the AKORD-12 analyzer. A similar system will be used for the CNPA-09 analyzer.

An example of the ion temperature profile reconstruction using a scanning analyzer in discharges nos. 38876, 78, 79, 86, 87 with the same parameters are shown in Fig. 9. The profile restoration method is

**Table 2.** Main parameters of charge exchange atom analyzers

Parameter	Parameter value		
	AKORD-12	AKORD-24M	CNPA-09
Number of energy channels $\times$ number of isotopes	$6 \times 2$	$12 \times 2$	$44 \times 1$
Energy range, keV for hydrogen	0.2–18	0.2–32	0.8–120
for deuterium	0.2–25	0.2–32	0.8–60
Dynamic range		7	hydrogen: 140 deuterium: 70
Energy channel width, %	9–40	9–25	4–90
Mass separation		0.01	0.01–0.001
Time resolution, ms		0.1	

described in [20]. For comparison, the figure shows the ion temperature profile obtained using the CXRS diagnostics. It can be seen that the agreement is good.

Figure 10 illustrates the use of neutral particle analyzers to study fast ion confinement. Figure 10a shows the experimental spectra of charge exchange atoms at 145 ms in the discharge no. 42630. The signal of the CNPA-09 analyzer is predominantly passive (integrated along the observation line), while the AKORD-24M analyzer is inclined with respect to the equatorial plane by approximately  $6^\circ$  downward and records predominantly a local spectrum in the region  $\rho = 0.46$  (where  $\rho$  is the normalized magnetic coordinate). Figure 10b shows the variation of the deuterium flux of 22.4 keV obtained using the AKORD-24M analyzer in the active measurement mode ( $\rho = 0.55$ ) and the deuterium atom flux of 28.6 keV obtained using the CNPA-09 analyzer in the mode with a pre-

dominantly passive signal during toroidal Alfvén modes. It can be seen that the signal along the observation line decreases, which indirectly indicates the loss of fast particles, while the peripheral active signal increases, which is associated with the transport of fast particles from the central region of the plasma closer to the boundary.

## 5. DIAGNOSTICS OF ACTIVE CHARGE EXCHANGE SPECTROSCOPY

Diagnostics of active charge exchange spectroscopy (or charge exchange recombination spectroscopy, CXRS) is based on the measurement and analysis of the spectral contour of the emission line (usually in the visible range) of hydrogen-like ions formed as a result of charge exchange of light impurity nuclei (He, B, C, N, O) on high-energy deuterium (or hydrogen) atoms injected into the plasma from a heating or diagnostic beam.

In the Globus-M2 tokamak, this diagnostic includes a specially developed optical system for collecting light along 7 “lines of sight” (LOS) in the equatorial plane of the facility (see Fig. 5) equipped with output SMA fiber connectors; a set of 20-meter SMA-SMA fiber-optic quartz cables with a diameter of  $400 \mu\text{m}$  with a numerical aperture  $NA = 0.22$  for transporting the light signal, a fiber-optic collector with SMA inputs and a special output lens that builds an image of the fibers at the input slit of a compact high-aperture high-resolution “SpectralTech” SPT-DDHR-04 spectrometer. This device is equipped with a  $154 \times 144 \text{ mm}$  grating with a cutting density of 1800 lines/mm and a glare angle of  $21^\circ$ , and mirror optics  $F = 280 \text{ mm } F/5.4$ , which make it possible to obtain a large dispersion of  $\sim 0.15 \text{ nm/mm}$  and wide operating range of 430–800 nm in the autocollimation scheme of double diffraction with grazing incidence ( $78^\circ$ ) [21]. An innovative, backlash-free positioning mechanism with software control makes it possible to perform the precise adjustment of the

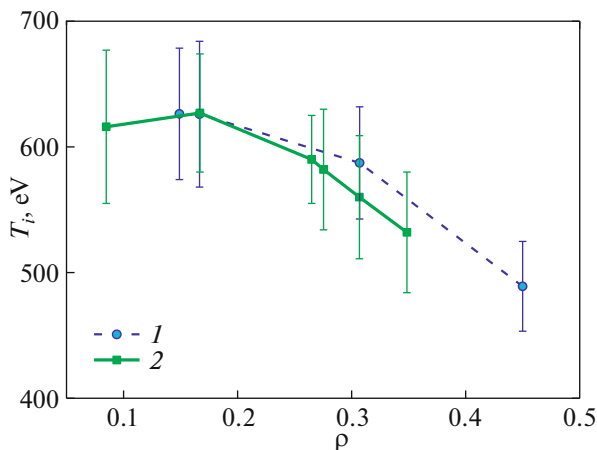


**Fig. 9.** Example of experimental ion temperature profiles obtained using the neutral particle analyzer and CXRS in discharges no. 38876, 78, 79, 86, 87 at time  $t = 200 \text{ ms}$ : (1) data from neutral particle analyzers; (2) diagnostic data of active charge exchange spectroscopy.

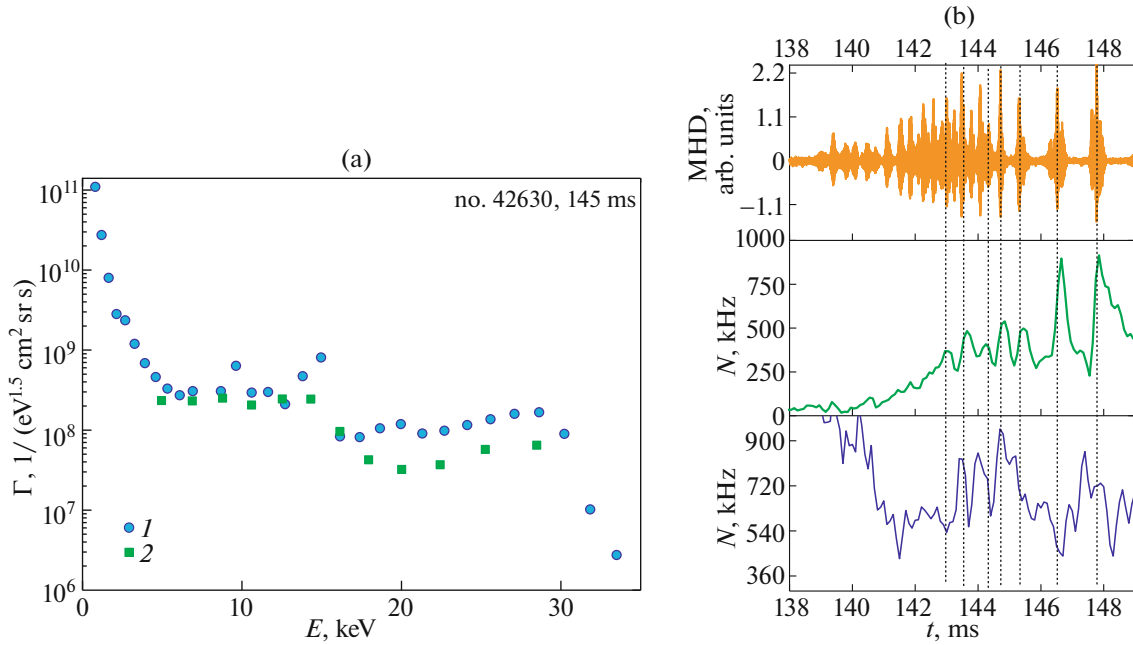


**Fig. 10.** Experimental spectra of deuterium atoms obtained using CNPA-09 (1) and AKORD-24M (2) analyzers in discharge no. 42630 (a); variation of the signal of neutral particle analyzers during toroidal Alfvén modes (b). From top to bottom: MHD probe signal, flux of 22.4-keV deuterium atoms obtained by the AKORD-24M analyzer in the active measurement mode, flux of 28.6-keV deuterium atoms obtained by the CNPA-09 analyzer in the mode with a predominantly passive signal.

wavelength, and also automatic scanning of any part of the spectrum over the entire operating range with an accuracy of  $\sim 0.0015$  nm. The output of the spectral device is equipped with a 16-bit recording system based on a cooled matrix CCD detector of  $512 \times 512$  pixels of  $16 \times 16$   $\mu\text{m}$  with the “frame transfer” architecture, which has the quantum efficiency  $QE > 95\%$  at 550 nm owing to the use of back-side illuminated technology (BSI) with anti-reflective coating. The resulting resolution of the spectrometer is  $\approx 0.0024$  nm/pixel, and the width of the hardware function FWHM is  $\approx 0.015$  nm at the input slit width of 100  $\mu\text{m}$ .

In the CXRS measurements, the emission line of the  $\text{C}^{5+}$  ion ( $n = 8 \rightarrow 7$ , 529.05 nm) was typically used because the main impurity in the Globus-M2 plasma is carbon owing to the graphite protection of the inner wall. The time resolution of the diagnostic was 5 ms. Table 3 shows the parameters for the location of the “lines of sight”: the values of the major radius of the

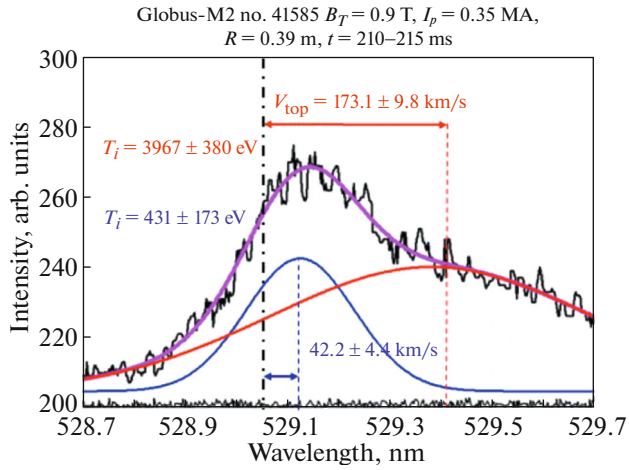
tokamak ( $R$ ) at the points of intersection of the LOS axis with the axis of the neutral beam, taking into account its finite width, and also the angle between the LOS axis and the toroidal direction at these points.

Figure 11 shows an example of a CXRS spectrum recorded in the discharge no. 41585 for LOS no. 2 at 210–215 ms (black line), and its approximation (purple curve) by the superposition of “active” charge exchange (red curve) and “passive” (blue curve) signals. The “passive” glow signal of the  $\text{C}^{5+}$  ion is concentrated in a narrow ( $\sim 1$ – $2$  cm) peripheral region of the plasma near the boundary approximately 1 cm from the separatrix.

Figure 12 shows the profiles of the ion temperature  $T_i(R)$  (a) and plasma toroidal rotation velocity  $V_{\text{tor}}(R)$  (b) measured on 210–215 ms of the discharge no. 42777. The ion temperature measurements using the CXRS diagnostics are consistent with the measurements using charge exchange atom analyzers (see Fig. 5) [2].

**Table 3.** Parameters for the location of “lines of sight” LOS

LOS number	1	2	3	4	5	76	7
$R$ , s	$36.2 \pm 1.4$	$39.3 \pm 0.8$	$42.4 \pm 0.4$	$45.3 \pm 0.4$	$48.2 \pm 0.3$	$50.8 \pm 0.3$	$53.2 \pm 0.4$
Angle between LOS axis and toroidal direction, degrees	6.1	2.2	0.2	−0.5	−0.1	0.6	1.9



**Fig. 11.** Measured CXRS spectrum (black line) and its approximation (purple line) with “active” (red) CX and “passive” (blue) signals in discharge no. 41585 at  $B_T = 0.9$  T and  $I_p = 0.35$  MA.

## 6. INTERFEROMETERS

The Globus-M2 tokamak has two interferometers for measuring the electron density. A microwave interferometer based on a backward wave lamp (BWL) operates at a probing wavelength of 1 mm. The interferometer provides the monitor measurements. Initially, probing was carried out along three vertical chords with a major radius  $R = 24, 42$  and  $50$  cm. Because of lamp aging and a drop in radiation power, now the interferometer can provide measurements only along one chord  $R = 42$  cm, which passes near the magnetic axis. The problem of replacing the generator with a solid-state one is under consideration owing to the lack of spare lamps. The first trial tests were carried out with a device provided to us by employees of the

Kurchatov Institute for temporary use. The issue of purchasing similar units is currently being considered.

The second interferometer is a recently commissioned dispersive interferometer (DI) based on a  $\text{CO}_2$  laser with an artificial phase modulation of probing radiation produced by the Budker Institute of Nuclear Physics, Siberian Branch, Russian Academy of Sciences, Novosibirsk, Russia [22]. A special measuring module was designed to record DI signals and calculate the real-time plasma density [23]. The plasma density calculation algorithms implemented in its digital unit are based on the harmonic analysis of interferometer signals, which makes them resistant to noise and changes in the modulation depth. The range of the noise component when measuring the linear density does not exceed  $\langle nl \rangle_{\min} \approx 6 \times 10^{12} \text{ cm}^{-2}$  with a time resolution of  $20 \mu\text{s}$ . The relative error in calculating the absolute value of the linear density does not exceed 2.5%. For both interferometers, the chord length for calculating the mean chord electron density is determined by restoring the position of the last closed magnetic surface using the current ring method [7].

In experiments on the Globus-M2 tokamak, two diagnostic systems were compared: the TS diagnostics and dispersive interferometry. The measurement chords of both diagnostics lie in the equatorial plane and have the same impact parameter and length. To compare the diagnostics, the mean chord electron density in TS was calculated using integration on the parameterized magnetic surfaces [24]. The comparison of TS and dispersive interferometer measurements in the discharge no. 42518 with  $n_e = (0.1\text{--}0.9) \times 10^{20} \text{ m}^{-3}$  (Fig. 13) show good agreement. Thus, dispersive interferometry diagnostics at the Globus-M2 tokamak produces reliable measurements of the mean chord electron density and is characterized by the high measurement accuracy in discharges with a high average plasma density, at least up to  $1.5 \times 10^{20} \text{ m}^{-3}$ .

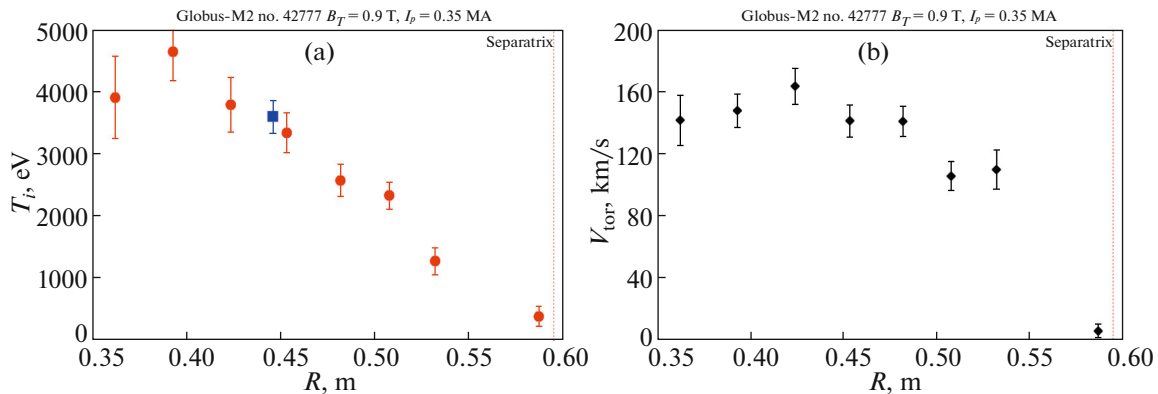


**Fig. 12.** Profiles of ion temperature (a) and toroidal rotation velocities of carbon  $\text{C}^{5+}$  ions in the plasma (b) at 210–215 ms of the discharge no. 42777 at  $B_T = 0.9$  T and  $I_p = 0.35$  MA. The blue square indicates the ion temperature measured using the AKORD-12 neutral particle analyzer.

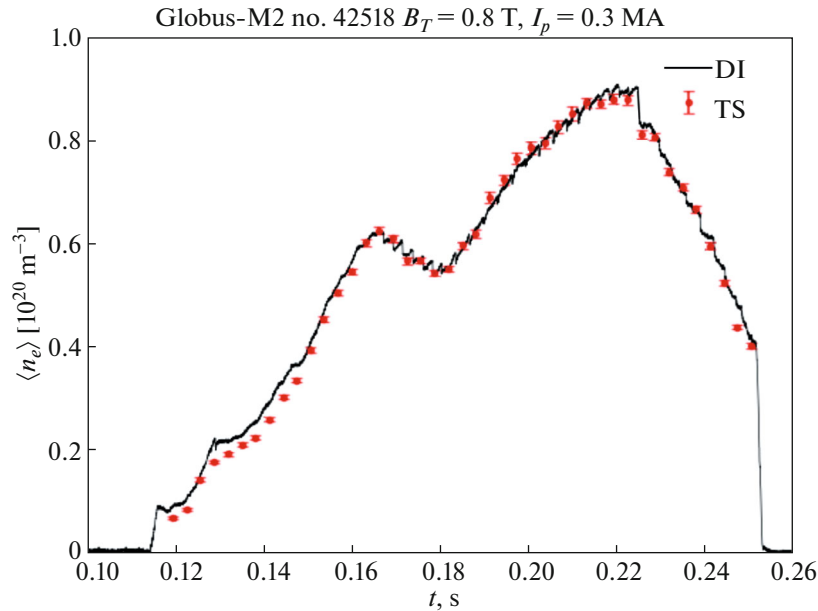


**Fig. 13.** Example of electron density measurements in the discharge no. 42518 of the Globus-M2 tokamak carried out by DI (black line) and Thomson scattering diagnostics (red dots).

## 7. DOPPLER REFLECTOMETER

Doppler backscattering (DBS) or Doppler reflectometry is a method for recording microwave radiation backscattered by plasma density fluctuations. This diagnostic makes it possible to determine the poloidal plasma rotation velocity from the measured frequency shift of scattered radiation, as well as to study plasma turbulence. The Globus-M2 tokamak uses three DOR microwave systems, the location of which and ray trajectories are shown in Fig. 4. The first system makes it possible to probe the plasma with one frequency, which can be varied in the range from 18 to 26 GHz between tokamak discharges. The second system probes the plasma simultaneously at four frequencies: 20, 29, 39, and 48 GHz. The third system operates at five frequencies: 50, 55, 60, 65, and 70 GHz. The frequency range of the reflectometer corresponds to the range of normalized minor radii  $\rho = 0.5\text{--}1.1$  depending on the experimental conditions.

The first and second systems use the technique of Doppler backscattering with dual homodyne detection. The operation of this scheme is described in detail in [25].

For the third system, a radiation frequency multiplier of a master oscillator with a radiation frequency of 5 GHz is used and heterodyne detection is applied. The operation of this scheme is described in more detail in [26].

Doppler backscattering diagnostic has several advantages. It allows measurements to be carried out locally, since backscattering occurs mainly at the cut-off due to the amplification of the microwave electric

field at the turning point of the ray path. In addition, the DBS method allows simultaneous measurements of the velocity and turbulence. This method implies the selectivity of measurements based on the wave vectors of scattering fluctuations. In addition, this method is relatively easy to use and multifunctional. Also, the DBS antenna system mounted at the Globus-M2 tokamak makes it possible to change the inclination angle, thereby allowing the use of standard reflectometry.

The transition to the improved confinement mode was studied at the Globus-M2 tokamak in detail using the DBS method [27]. In addition, the DBS method has been widely used to study plasma processes listed in Table 4 [28].

## 8. NEUTRON DIAGNOSTICS

To record neutron fluxes, the Globus-M2 tokamak is equipped with two compact neutron spectrometers based on the BC-501A liquid organic scintillator, and also two  $^{10}\text{B}$  corona neutron counters. The neutron diagnostic is mainly applied to studying the confinement of fast ions arising during heating the plasma by high-energy atomic beams, and also to estimate the integral neutron yield. The signal from neutron spectrometers is digitized at a frequency of 500 MHz, and the maximum input load is  $\sim 1 \times 10^6 \text{ s}^{-1}$ . The signal from neutron counters is digitized with a frequency of 30 MHz, and the maximum input load is  $\sim 6 \times 10^4 \text{ s}^{-1}$ . The signal level at the detectors can be adjusted using lead and polyethylene collimators. The location of neutron detectors in the experimental hall is shown in

**Table 4.** Plasma processes studied using DBS diagnostics

Phenomenon	Certain characteristics
Turbulence	Suppression of turbulence by the velocity shear, correlation lengths of turbulent structures
Geodesic acoustic mode (GAM)	Amplitude of electric field oscillations, localization, degree of nonlinear interaction with turbulence
Limiting cycle oscillations (LCO)	Speed shear at LCO, turbulence modulation, localization
Filaments	Radial and poloidal size, distance between filaments, propagation speed, development area, mode structures
Alfvén modes	Frequency, amplitude of magnetic field oscillations, localization
Tearing modes	Frequency, localization

Fig. 14. The neutron diagnostic complex of the Globus-M2 tokamak was discussed in detail in [29].

In the Globus-M2 plasma, neutrons are produced during collisions of high-energy ions with thermal ions of the main plasma, as well as with each other. Thus, the development of processes leading to the loss of fast particles or their redistribution in the phase space in the plasma causes a change in the neutron flux. An example of the response of the signal of neutron detec-

tors to sawtooth oscillations and toroidal Alfvén eigenmodes (TAE) is shown in Fig. 15.

To estimate the integral neutron yield from the tokamak plasma, the neutron detectors were absolutely calibrated under the conditions of the experimental hall of the facility [30]. An example of the evolution of the integral neutron yield in one of the discharges of the Globus-M2 tokamak is shown in Fig. 16a. The response functions of BC-501A neutron spectrometers were measured to calculate the energy spectrum of neutrons emitted by the plasma at the cyclotron of the Ioffe Institute [31]. Based on them, a procedure for the deconvolution of experimentally measured spectra was carried out [32]. An example of the reconstructed energy spectrum of emitted neutrons is shown in Fig. 16b.

Currently, two more  $\text{He}^3$  proportional neutron counters are being put into operation in addition to the neutron detectors described in this section.

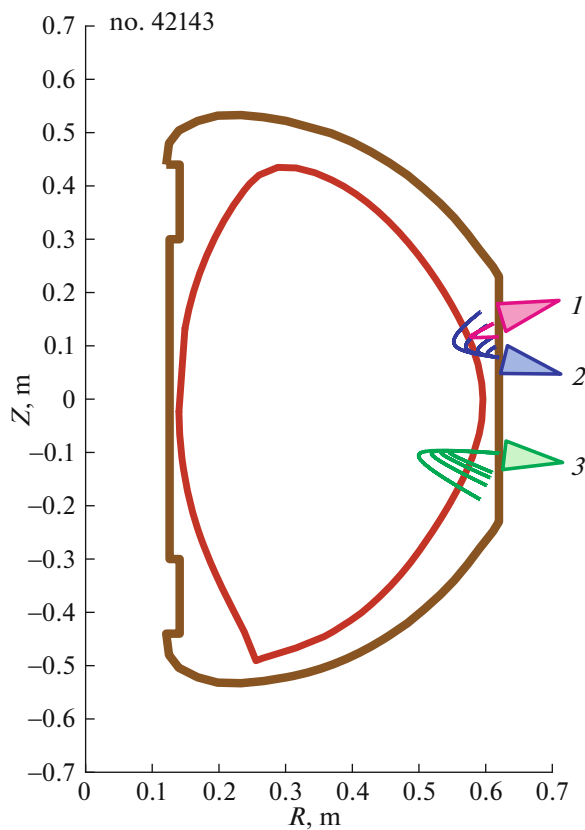


**Fig. 14.** Results of ray path calculations for three DBS systems.

## 9. HARD X-RAY DIAGNOSTICS

To study hard X-ray signals, the tokamak is equipped with two absolutely calibrated scintillation spectrometers based on the  $\text{LaBr}_3(\text{Ce})$  crystal [33]. The measurements are carried out in the range of gamma quanta energies of 0.1–16 MeV with a digitization frequency of the recorded signal of 250 MHz at a maximum input statistical load of  $\sim 3 \times 10^6 \text{ s}^{-1}$ . The measured spectra can be used to study the behavior of runaway electrons. An example of hard X-ray signal evolution during the low-density ohmic discharge ( $\langle n_e \rangle = 1.7 \times 10^{19} \text{ m}^{-3}$ ) is shown in Fig. 17a. Figure 17b shows the energy spectrum of gamma quanta recorded in the same discharge.

To control the level of hard X-ray radiation during a discharge, the tokamak is also equipped with a scintillation detector based on a  $\text{NaI}(\text{Tl})$  crystal operating in the current mode.

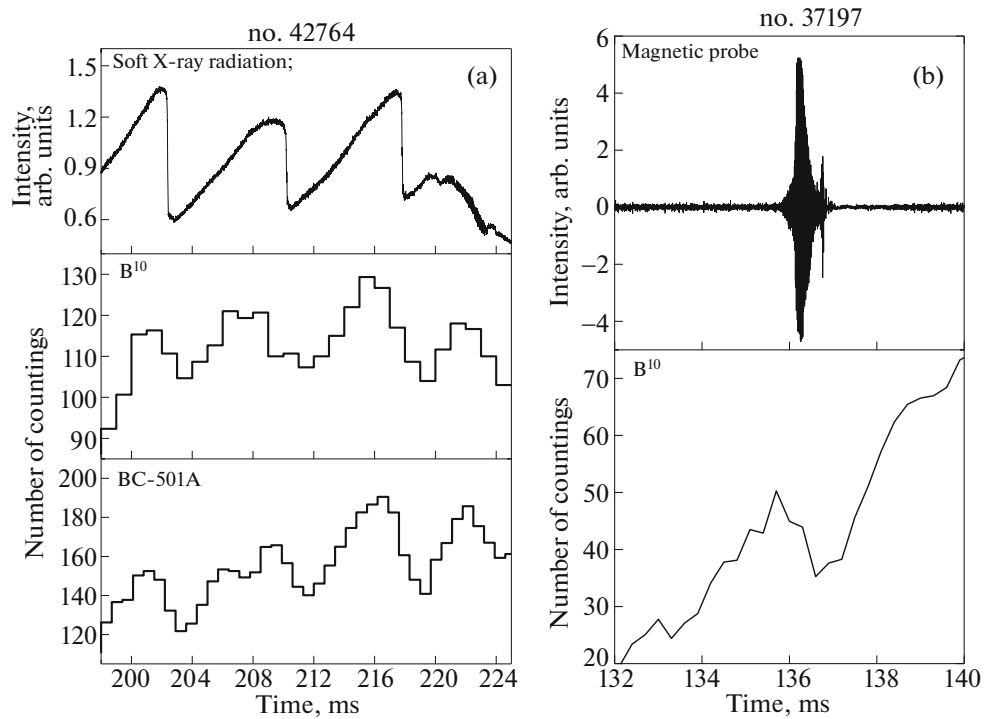


**Fig. 15.** Time dependence of the neutron flux in a discharge with sawtooth oscillations (a), and in a discharge with TAE (b).

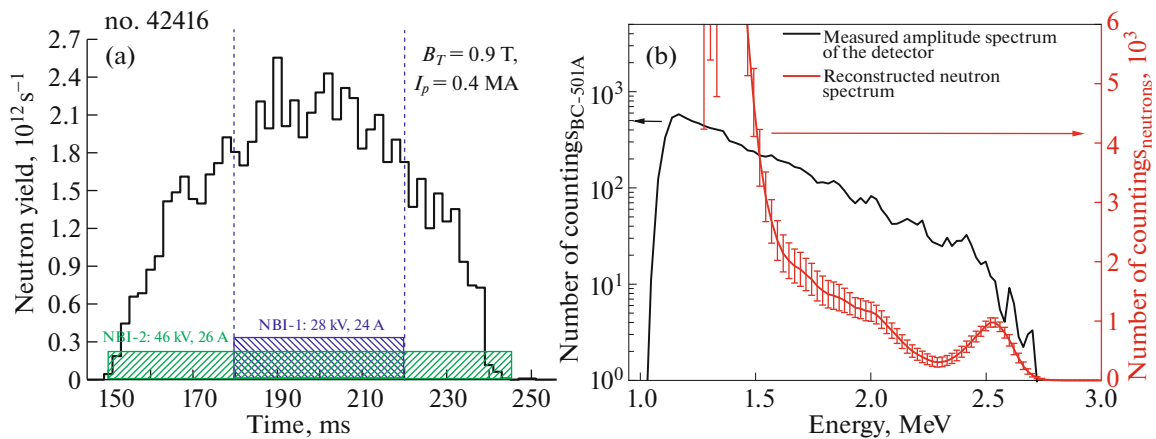


**Fig. 16.** Time dependence of the neutron yield in the discharge no. 42416 of the Globus-M2 tokamak (a), experimentally measured spectrum (black line), and reconstructed neutron spectrum from the Globus-M2 tokamak plasma (red line) (b).

## 10. SPECTROSCOPIC DIAGNOSTICS

A complex of spectroscopic diagnostics at the Globus-M2 tokamak is used to obtain data on the behavior of impurities in the plasma based on radiation intensity measurements in the range from 0.02 to 1200 nm. The complex includes diagnostics of mean chord effective charge  $\langle Z_{\text{eff}} \rangle$ , diagnostics of individual lines of impurity elements, a survey spectrometer, mono-

chromators for multi-angle radiation intensity measurements on the  $D\alpha/H\alpha$  line and silicon photodiodes (SPD) for radiation power measurements in a wide range of 0.02–1100 nm.

The mean chord value of the effective charge  $\langle Z_{\text{eff}} \rangle$  is determined by the bremsstrahlung radiation intensity simultaneously in two spectral intervals of 1019–1040 and 630–640 nm, where there is no intense line radiation (recombination radiation under measure-

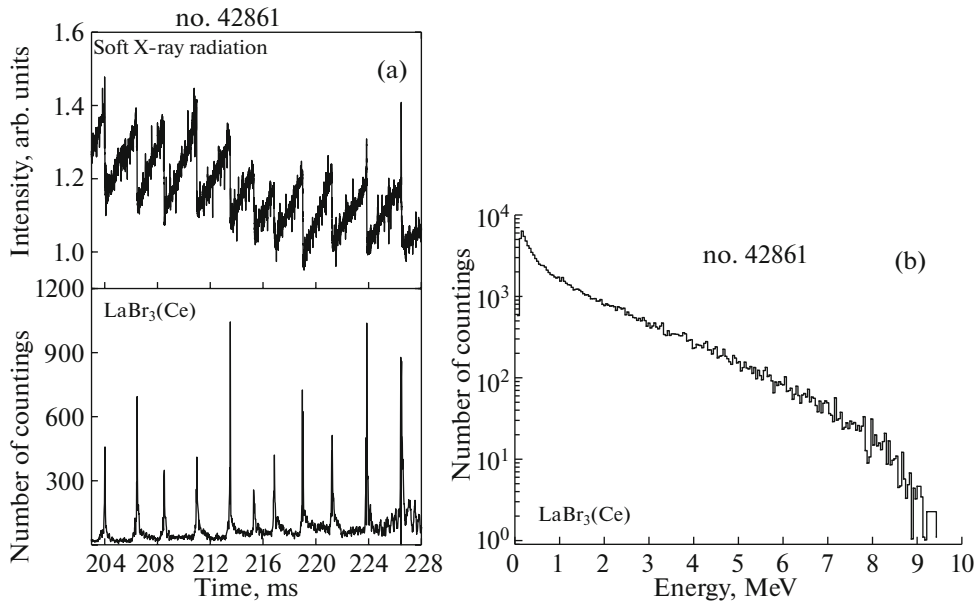


**Fig. 17.** Discharge no. 42861: time dependence of the hard X-ray signal during the ohmic discharge of the Globus-M2 tokamak (a), and experimentally measured energy of hard X-ray spectrum (b).

ment conditions is negligible). The bremsstrahlung power  $P_{br}$  is measured along one observation chord in the equatorial section of the Globus-M2 tokamak [34]. To calculate  $\langle Z_{eff} \rangle$  according to  $P_{br}$ ,  $T_e(R)$  and  $n_e(R)$  profiles are used obtained by Thomson scattering (TS) diagnostics [12] and converted into flux coordinates using a 0-dimensional model [13], as well as magnetic reconstruction data using the current ring method [7]. The bremsstrahlung power is measured in the monitor mode (data in the public domain is updated after each discharge), the  $\langle Z_{eff} \rangle$  value can be calculated within several minutes once the  $T_e(R)$  and  $n_e(R)$  profiles and magnetic reconstruction are obtained. The time resolution is determined by the laser pulse repetition rate of the TS diagnostics of 330 Hz and provides the measurements of  $\langle Z_{eff} \rangle$  with a step of 3.03 ms.

Using six filter monochromators tuned to individual spectral lines, the input of each of the main impurity C, O, Fe, N, B and He elements into the plasma is monitored. The data acquisition system allows recording monochromator signals over the entire discharge with a digitization frequency of up to 1 MHz in the monitor mode. Emission from impurity lines is recorded in an observation volume with a diameter of about 5 mm along the observation chord in the equatorial plane of the tokamak (Fig. 18). In special cases, e.g., when an impurity is introduced into the divertor region, the observation angle of the monochromators can be changed.

The survey emission spectra in the range of 200–1100 nm can also be measured using a system based on the Avantes AvaSpec-ULS2048 spectrometer (see Fig. 1). Spectra can be recorded every 1.05 ms. The integration time can be increased for a detailed consideration of weaker lines. The survey spectra are also recorded in the monitor mode and are available after each discharge. Figure 19 shows a characteristic view of the emission spectrum measured using a survey spectrometer, with the indicated spectral intervals in which impurity lines are recorded by filter monochromators.

The radiation intensity of the  $D\alpha/H\alpha$  line at a wavelength of 656 nm is measured using five filter monochromators in five different observation angles: two chords oriented towards the upper and lower dome of the camera, two vertical chords pass through major radius  $R = 42$  and 50 cm, and one chord is oriented in the direction of a major radius to the central column. The measurements are also made in the monitor mode.

To measure the plasma radiation power at the tokamak, SPD photodiodes are used [35], which allow measurements in a wide spectral range of 1 eV–60 keV with a time resolution of up to 1  $\mu$ s. These photodiodes can be sensitive to radiation and particles [36]. Currently, the measurements from three angles are available: a survey device with an observation line directed tangentially to the plasma cord, with a wide radiation collection angle; two collimated sensors have observation lines directed along the major radius and tangentially in the peripheral region.

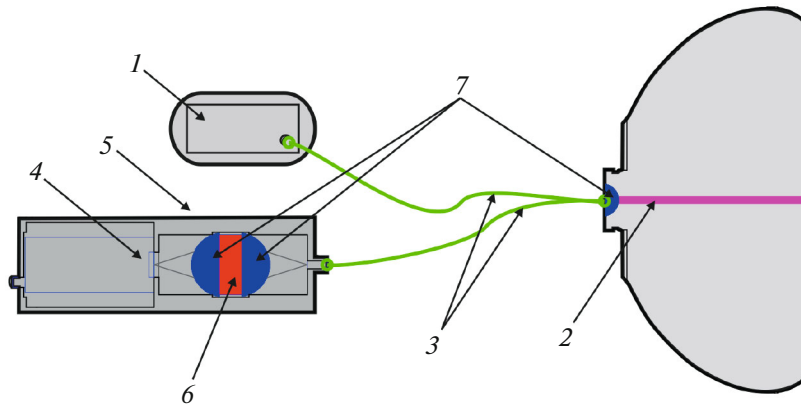


**Fig. 18.** Scheme for recording radiation intensity using filter monochromators and a survey spectrometer: (1) survey spectrometer, (2) observation region, (3) optical fiber, (4) detector, (5) collimator, (6) interference filter, (7) collecting lenses.

## 11. SOL REGION DIAGNOSTICS

The Globus-M2 tokamak has a number of diagnostics designed to study plasma in the boundary layer region between the separatrix and the wall (SOL). Their location is shown in Fig. 20.

A movable Langmuir probe [37] is located in the equatorial plane on the low-magnetic-field side and is equipped with a head with nine graphite electrodes in a boron nitride insulator. The probe makes it possible to measure the floating potential ( $V_f$ ), ion saturation current ( $I_{sat}$ ), electron density ( $n_e$ ), and temperature ( $T_e$ ), and also Mach number ( $M_{||}$ ). The probe head is placed in a protective graphite screen. The probe is driven by a linear magnetic manipulator, which makes it possible to change the position of the probe along

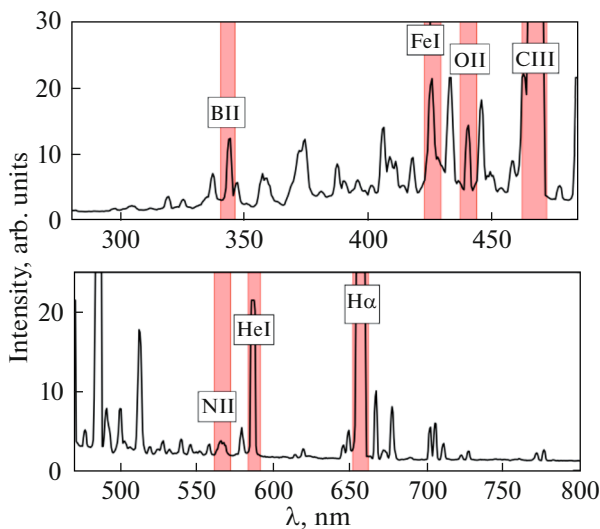


**Fig. 19.** Emission spectrum measured using a survey spectrometer with the indicated spectral intervals, in which impurity lines are recorded by filter monochromators.

a minor radius from discharge to discharge (which was used to obtain profiles of the measured parameters), and also provides 360° rotation of the head around the longitudinal axis. Figure 21 shows an example of the electron temperature and concentration profiles measured using a movable probe. The characteristic decay lengths of temperature ( $\lambda_{Te}$ ) and density ( $\lambda_{ne}$ ) are determined from the profiles for comparison with scalings.

The IR camera (thermal imager) [10] is located on the upper dome of the vacuum vessel at a distance of 1.3 m from the lower divertor plates, to which it is directed. The  $Cd_xHg_{1-x}Te$  IR detector provides operation in the wavelength range of 3.5–4.7  $\mu m$ , the frame size is  $320 \times 256$  pixels in the full frame mode, which corresponds to a spatial resolution of  $\sim 1.6$  mm/pixel with a frequency of  $\sim 220$  Hz. This diagnostic makes it possible to measure the evolution of the surface temperature of divertor plates and, based on the data obtained, to restore the heat flux density. In some experiments, the camera was mounted in the equatorial plane to observe the heating of the vessel wall on the outer bypass. Figure 22 shows an emergency incident filmed by a camera, when during a discharge a protective graphite plate came off from the central column (on the left in the figure) and flew to the outer wall. The three phases of its flight are visible in the figure.

Along with the IR camera, an IR pyrometer is used to measure the wall temperature. It makes it possible to measure the thermal radiation intensity in the temperature range of 100–3500°C with a time resolution of 2  $\mu s$ . It differs from a thermal imager in its higher time resolution. The combined use of a pyrometer and a thermal imager makes it possible to record the spatial distribution and the dynamics of the absolute surface temperature value. More details about the design of the IR pyrometer can be found in [38].

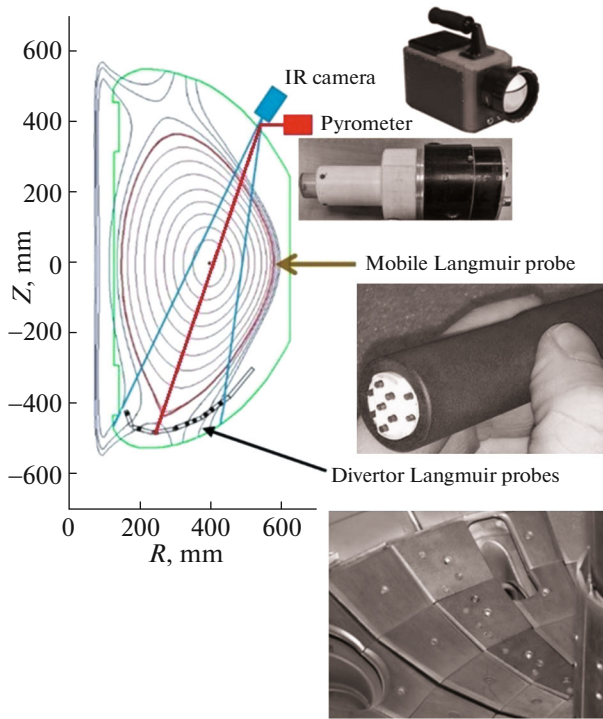


Fig. 20. SOL diagnostics on the Globus-M2 tokamak.

A set of ten Langmuir probes is mounted in the lower divertor plates [39]. The probes are made of the same grade of RGT-91 graphite as the plates, and have a flat working surface, the distance between them is 2 cm on average. The diameter of the probes is 8 mm, the gap between the plate and the probe is 0.5 mm, isolation from the divertor plates is carried out by using ceramic rings. For this array of probes, a recording system has been developed that can operate in three modes: the measurement of ion saturation current, measurement of the floating potential of the probes and recording of the probe current-voltage characteristic.

## 12. FOIL SOFT X-RAY SPECTROMETER

The spectrometer is designed for the continuous measurement of soft X-ray radiation (SXR) from the center of the tokamak plasma. Four channels with beryllium foils of various thicknesses (15, 50, 80, and 127  $\mu\text{m}$ ) allow the data obtained to be used to determine the central electron temperature with a time resolution of 3  $\mu\text{s}$ . However, the electron temperature determined by the classical “foil method” [40] from the ratio of signals in different channels in many cases differs greatly from that measured by the Thomson scattering diagnostics. This is apparently due to the significant contribution of line emission to the SXR signals. To improve the situation, a machine learning (ML) method was applied [41]. The training data included the results of measurements of the flux intensity of soft and hard X-rays, and also the emission of carbon impurities on the CIII line. The central electron temperature data obtained by the Thomson scattering diagnostics were used as responses for supervised learning. As a result, using ML from SXR signals it is possible to determine the electron temperature with an accuracy of 18%. In our case, the method is applicable to determine  $T_e$  in the range from  $\sim 300$  to  $\sim 1200$  eV. To measure higher electron temperatures, it is necessary to expand the spectral range of the SXR diagnostics and conduct a training cycle using new data.

## 13. HIGH SPEED VIDEO CAMERA

To visualize processes in the plasma of the Globus-M2 tokamak, a high-speed Optronis camera is used, which allows video recording at a speed of 540 frames/s with a resolution of  $1696 \times 1710$  to 100000 frames/s with a resolution of  $96 \times 38$  throughout the entire discharge. The continuous recording time with 8 GB of memory is 5.5 s. The camera is used to observe the plasma boundary and compare video data of the plasma with the reconstruction of the extreme magnetic surface obtained from magnetic

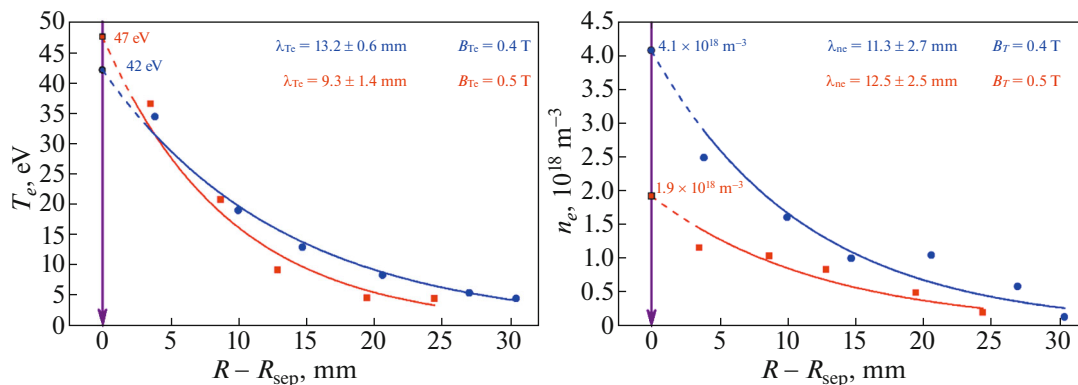
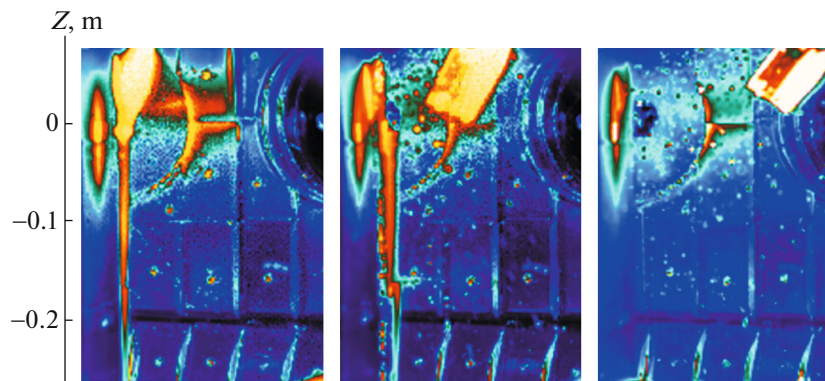
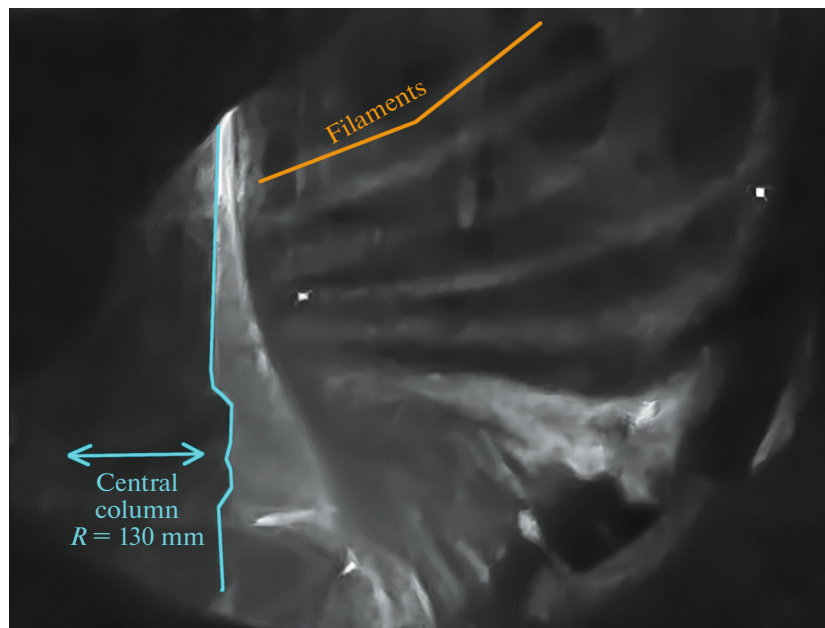


Fig. 21. Temperature and density profiles obtained using a movable probe.



**Fig. 22.** Separation of the protective graphite plate, which is recorded using a thermal imager in discharge no. 42422.



**Fig. 23.** Post-processed high-speed camera frame from discharge no. 29874 demonstrating the filamentous structure that occurs during the development of edge instability (edge-localized mode).

measurements using equilibrium codes. In addition, the camera is used to observe external influences on the plasma, such as gas injection, penetration of the plasma gun jet and dust particles. The possibility of using high-speed video recording in the visible radiation range to analyze the structure of the peeling-ballooning mode during the development and breakdown of edge MHD instabilities was also studied. Figure 23 shows a video camera frame obtained after special processing. The shooting speed was 1000 frames/s, and the exposure time was 300  $\mu\text{s}$ . To increase the contrast of the filaments, the background signal was subtracted and the pixel intensity values were multiplied by a constant value. The frame clearly demonstrates the development of the edge instability synchronized with reconnections [42]. The frequency of shooting frames

was 2.5 times higher than the frequency of reconnections, so it was possible to subtract the background by subtracting the previous frame.

#### 14. CONCLUSIONS

Currently, the diagnostic complex of the Globus-M2 tokamak represents an extensive set of diagnostics of various types, mutually complementing each other. Some of the diagnostics provide monitor measurements of the main characteristics of the plasma discharge, allowing the experimenter to monitor the reproducibility of the discharge during the experiment or controllably change the parameters of interest to him/her. Advanced diagnostics provide measurements of radial profiles of such quantities as electron and ion

temperature, plasma density, rotation speed, effective charge, radiation in the visible and soft X-ray range. Some diagnostic data require additional processing. The measurement results are used to simulate transport processes. A number of diagnostics provide data on the confinement and loss of fast particles that occur when using additional plasma heating methods.

The tokamak diagnostic complex is constantly being improved. This happens via the development of existing diagnostics and the creation of new ones. Thus, in the Thomson scattering diagnostics, the number of spatial points on the profile increases; in the CXRS diagnostics, a second observation angle appears, focused on working with the beam of the new injector. It is planned to install an SXR pinhole camera with the observation from two angles in a single poloidal cross section, which will provide tomographic measurements.

#### ACKNOWLEDGMENTS

The experiments were carried out on the unique Globus-M spherical tokamak device, which is a part of the Federal Center for Collective Use of the Ioffe Institute, Russian Academy of Sciences, “Materials Science and Diagnostics in Advanced Technologies.”

#### FUNDING

The development of the Thomson scattering diagnostics for the Globus-M2 tokamak diverter and the pilot electron temperature measurements (Section 3) were supported by the Russian Science Foundation (project no. 23-79-00033). The measurements using a laser interferometer (Section 6) were supported by the Russian Science Foundation (project no. 21-79-20201). The work on the preparation of poloidally spaced DBS systems (Section 7) for the study of filaments was supported by the Russian Science Foundation (grant no. 23-72-00024, <https://rscf.ru/project/23-72-00024>). The study of fast particles using a charge exchange atom analyzer (Section 4) and neutron diagnostics (Section 8) was supported by the Russian Science Foundation (project no. 21-72-20007). The development of the foil spectrometer (Section 12) was supported by the State assignment of the Ioffe Institute (no. 0040-2019-0023). The development of diagnostics for active charge exchange spectroscopy (Section 5) was supported by the contract 0034-2021-0001.

#### CONFLICT OF INTEREST

The authors of this work declare that they have no conflicts of interest.

#### REFERENCES

1. V. B. Minaev, V. K. Gusev, N. V. Sakharov, V. I. Varfolomeev, N. N. Bakharev, V. A. Belyakov, E. N. Bondarchuk, P. N. Brunkov, F. V. Chernyshev, V. I. Davydenko, V. V. Dyachenko, A. A. Kavin, S. A. Khitrov, N. A. Khromov, E. O. Kiselev, et al., *Nucl. Fusion* **57**, 066047 (2017). <https://doi.org/10.1088/1741-4326/aa69e0>
2. G. S. Kurskiev, I. V. Miroshnikov, N. V. Sakharov, V. K. Gusev, Yu. V. Petrov, V. B. Minaev, I. M. Balachenkov, N. N. Bakharev, F. V. Chernyshev, V. Yu. Goryainov, A. A. Kavin, N. A. Khromov, E. O. Kiselev, S. V. Krikunov, K. M. Lobanov, et al., *Nucl. Fusion* **62**, 104002 (2022). <https://doi.org/10.1088/1741-4326/ac881d>
3. V. V. D'yachenko, M. A. Irzak, E. N. Tregubova, and O. N. Shcherbinin, *Tech. Phys.* **48**, 1061 (2003). <https://doi.org/10.1134/1.1607482>
4. V. V. Dyachenko, O. N. Shcherbinin, E. Z. Gusakov, V. K. Gusev, M. A. Irzak, G. S. Kurskiev, Yu. V. Petrov, A. N. Saveliev, N. V. Sakharov, S. A. Khitrov, N. A. Khromov, V. I. Varfolomeev, and A. V. Voronin, *Nucl. Fusion* **55**, 113001 (2015).
5. E. O. Kiselev, I. M. Balachenkov, N. N. Bakharev, V. I. Varfolomeev, A. V. Voronin, V. Yu. Goryainov, V. K. Gusev, N. S. Zhiltsov, O. A. Zenkova, G. S. Kurskiev, A. D. Melnik, V. B. Minaev, I. V. Miroshnikov, M. I. Patrov, Yu. V. Petrov, et al., *Plasma Phys. Rep.* **49**, 1490 (2023).
6. S. A. Galkin, A. A. Ivanov, S. Yu. Medvedev, and Yu. Yu. Poshekhonov, *Nucl. Fusion* **37**, 1455 (1997). <https://doi.org/10.1088/0029-5515/37/10/I11>
7. V. I. Vasiliev, Yu. A. Kostsov, K. M. Lobanov, L. P. Makarova, A. B. Mineev, V. K. Gusev, R. G. Levin, Yu. V. Petrov, and N. V. Sakharov, *Nucl. Fusion* **46**, S625 (2006). <https://doi.org/10.1088/0029-5515/46/8/S08>
8. L. L. Lao, H. St. John, R. D. Stambaugh, and W. Pfeiffer, *Nucl. Fusion* **25**, 1421 (1985). <https://doi.org/10.1088/0029-5515/25/10/004>
9. A. Yu. Yashin, A. M. Ponomarenko, I. M. Balachenkov, G. S. Kurskiev, E. O. Kiselev, V. B. Minaev, A. V. Petrov, Yu. V. Petrov, N. V. Sakharov, and N. S. Zhiltsov, *Appl. Sci.* **13**, 3430 (2023). <https://doi.org/10.3390/app13063430>
10. Yu. V. Petrov, V. K. Gusev, N. V. Sakharov, V. B. Minaev, V. I. Varfolomeev, V. V. D'yachenko, I. M. Balachenkov, N. N. Bakharev, N. N. Bondarchuk, V. V. Bulanin, F. V. Chernyshev, M. V. Iliasova, A. A. Kavin, E. M. Khilkevitch, N. A. Khromov, et al., *Nucl. Fusion* **62**, 042009 (2022). <https://doi.org/10.1088/1741-4326/ac27c7>
11. I. M. Balachenkov, Yu. V. Petrov, V. K. Gusev, N. N. Bakharev, V. I. Varfolomeev, V. V. D'yachenko, A. N. Konovalov, P. A. Korepanov, S. V. Krikunov, V. B. Minaev, M. I. Patrov, and N. V. Sakharov, *Pis'ma Zh. Tekh. Fiz.* **47** (12), 17 (2021). <https://doi.org/10.21883/PJTF.2021.12.51061.18730>
12. G. S. Kurskiev, N. S. Zhiltsov, A. N. Koval, A. F. Kornev, A. M. Makarov, E. E. Mukhin, Yu. V. Petrov, N. V. Sakharov, V. A. Solovei, E. E. Tkachenko, S. Yu. Tolstyakov, and P. V. Chernakov, *Tech. Phys. Lett.* **48** (15), 78 (2022). <https://doi.org/10.21883/TPL.2022.15.54273.19019>
13. G. S. Kurskiev, N. V. Sakharov, P. B. Shchegolev, N. N. Bakharev, E. O. Kiselev, G. F. Avdeeva, V. K. Gu-

- sev, A. D. Ibyaminova, V. B. Minaev, I. V. Miroshnikov, M. I. Patrov, Yu. V. Petrov, A. Yu. Tel'nova, S. Yu. Tolstyakov, and V. A. Tokarev, *Vopr. At. Nauki Tekh., Ser.: Termoyad. Sint.* **39** (4), 86 (2016).
14. N. S. Zhiltsov, G. S. Kurskiev, S. Yu. Tolstyakov, V. A. Solovey, A. N. Koval, S. E. Aleksandrov, A. N. Bazhenov, P. V. Chernakov, S. V. Filippov, V. K. Gusev, N. A. Khromov, E. O. Kiselev, A. F. Kornev, S. V. Krikunov, A. M. Makarov, et al., arXiv:2311.18723. <https://doi.org/10.48550/arXiv.2311.18723>.
  15. N. V. Ermakov, N. S. Zhiltsov, G. S. Kurskiev, E. E. Mukhin, S. Yu. Tolstyakov, E. E. Tkachenko, V. A. Solovey, I. V. Bocharov, K. V. Dolgova, A. A. Kavin, A. N. Koval, K. O. Nikolaenko, A. N. Novokhatsky, Yu. V. Petrov, V. A. Rozhansky, et al., *Plasma Phys. Rep.* **49**, 1480 (2023).
  16. A. B. Izvozchikov, M. P. Petrov, S. Ya. Petrov, F. V. Chernyshev, and I. V. Shustov, *Tech. Phys.* **37**, 201 (1992).
  17. F. V. Chernyshev, V. I. Afanasyev, A. V. Dech, M. Kick, A. I. Kislyakov, S. S. Kozlovskii, A. Kreter, M. I. Mironov, M. P. Petrov, and S. Ya. Petrov, *Instrum. Exp. Tech.* **47**, 214 (2004).
  18. N. N. Bakharev, A. D. Melnik, and F. V. Chernyshev, *Atoms* **11**, 53 (2023). <https://doi.org/10.3390/atoms11030053>
  19. N. N. Bakharev, I. M. Balachenkov, F. V. Chernyshev, V. K. Gusev, E. O. Kiselev, G. S. Kurskiev, A. D. Melnik, V. B. Minaev, M. I. Mironov, V. G. Nesenevich, Yu. V. Petrov, N. V. Sakharov, P. B. Shchegolev, O. M. Skrekel, A. Yu. Telnova, et al., *Plasma Phys. Controlled Fusion* **63**, 125036 (2021). <https://doi.org/10.1088/1361-6587/ac3497>
  20. N. N. Bakharev, F. V. Chernyshev, V. K. Gusev, E. O. Kiselev, G. S. Kurskiev, M. M. Larionova, A. D. Melnik, V. B. Minaev, M. I. Mironov, I. V. Miroshnikov, Yu. V. Petrov, N. V. Sakharov, P. B. Shchegolev, O. M. Skrekel, A. Yu. Telnova, et al., *Plasma Phys. Controlled Fusion* **62**, 125010 (2020). <https://doi.org/10.1088/1361-6587/abbe32>
  21. Yu. S. Koshkin, E. E. Mukhin, G. T. Razdobarin, V. V. Semenov, A. Shilnikov, Yu. K. Mihailovskij, and L. I. Bakh, *Rev. Sci. Instrum.* **70**, 3844 (1999). <https://doi.org/10.1063/1.1149999>
  22. S. V. Ivanenko, A. L. Solomakhin, N. S. Zhil'tsov, P. V. Zubarev, Yu. V. Kovalenko, G. S. Kurskiev, V. V. Solokha, E. E. Tkachenko, K. D. Shulyat'ev, E. A. Puryga, A. D. Khil'chenko, V. B. Minaev, and P. A. Bagryanskii, *Vopr. At. Nauki Tekh., Ser.: Termoyad. Sint.* **46** (1), 86 (2023).
  23. S. V. Ivanenko, K. A. Grinemaier, E. A. Puryga, A. N. Kvashnin, and P. A. Bagryanskii, *Vopr. At. Nauki Tekh., Ser.: Termoyad. Sint.* **45** (1), 67 (2022).
  24. G. S. Kurskiev, N. V. Sakharov, P. B. Schegolev, N. N. Bakharev, E. O. Kiselev, G. F. Avdeeva, V. K. Gusev, A. D. Ibyaminova, V. B. Minaev, I. V. Miroshnikov, M. I. Patrov, Yu. V. Petrov, A. Yu. Telnova, S. Yu. Tolstyakov, and V. A. Tokarev, *Phys. At. Nucl.* **80**, 1313 (2017).
  25. V. V. Bulanin, A. Y. Yashin, A. V. Petrov, V. K. Gusev, V. B. Minaev, M. I. Patrov, Y. V. Petrov, D. V. Prisiazhniuk, and V. I. Varfolomeev, *Rev. Sci. Instrum.* **92**, 033539 (2021). <https://doi.org/10.1063/5.0030307>
  26. A. Y. Yashin, V. V. Bulanin, V. K. Gusev, V. B. Minaev, A. V. Petrov, Y. V. Petrov, A. M. Ponomarenko, and V. I. Varfolomeev, *J. Instrum.* **17**, C01023 (2022). <https://doi.org/10.1088/1748-0221/17/01/C01023>
  27. A. Ponomarenko, A. Yashin, G. Kurskiev, V. Minaev, A. Petrov, Y. Petrov, N. Sakharov, and N. Zhiltsov, *Sensors* **23**, 830 (2023). <https://doi.org/10.3390/s23020830>
  28. A. Yashin, V. Bulanin, A. Petrov, and A. Ponomarenko, *Appl. Sci.* **11**, 8975 (2021). <https://doi.org/10.3390/app11198975>
  29. M. V. Iliasova, A. E. Shevelev, E. M. Khilkevitch, N. N. Bakharev, O. M. Skrekel, V. B. Minaev, D. N. Doinikov, D. B. Gin, V. K. Gusev, V. A. Kornev, V. O. Naidenov, A. N. Novokhatskii, Yu. V. Petrov, I. A. Polunovsky, N. V. Sakharov, et al., *Nucl. Instrum. Methods Phys. Res., Sect. A* **1029**, 166425 (2022). <https://doi.org/10.1016/j.nima.2022.166425>
  30. O. M. Skrekel, N. N. Bakharev, V. I. Varfolomeev, V. K. Gusev, M. V. Ilyasova, A. Yu. Telnova, E. M. Khilkevitch, and A. E. Shevelev, *Tech. Phys.* **67** (1), 12 (2022). <https://doi.org/10.21883/TP.2022.01.52526.151-21>
  31. M. V. Iliasova, A. E. Shevelev, E. M. Khilkevitch, I. N. Chugunov, V. B. Minaev, D. B. Gin, D. N. Doinikov, I. A. Polunovsky, V. O. Naidenov, M. A. Kozlovskiy, and M. F. Kudoyarov, *Nucl. Instrum. Methods Phys. Res., Sect. A* **983**, 164590 (2020). <https://doi.org/10.1016/j.nima.2020.164590>
  32. E. M. Khilkevitch, A. E. Shevelev, I. N. Chugunov, M. V. Iliasova, D. N. Doinikov, D. B. Gin, V. O. Naidenov, and I. A. Polunovsky, *Nucl. Instrum. Methods Phys. Res., Sect. A* **977**, 164309 (2020). <https://doi.org/10.1016/j.nima.2020.164309>
  33. A. E. Shevelev, I. N. Chugunov, V. K. Gusev, Yu. V. Petrov, V. V. Rozhdestvenskii, A. B. Mineev, N. V. Sakharov, D. N. Doinikov, A. L. Izotov, S. V. Krikunov, V. O. Naidenov, K. A. Podushnikova, I. A. Polunovskii, D. B. Gin, and A. I. Chugunov, *Plasma Phys. Rep.* **30**, 159 (2004). <https://doi.org/10.1134/1.1648942>
  34. E. A. Tukhmenova, S. Yu. Tolstyakov, G. S. Kurskiev, V. K. Gusev, V. B. Minaev, Yu. V. Petrov, N. V. Sakharov, A. Yu. Telnova, N. N. Bakharev, P. B. Shchegolev, and E. O. Kiselev, *Plasma Sci. Technol.* **21**, 105104 (2019). <https://doi.org/10.1088/2058-6272/ab305f>
  35. A. P. Artyomov, E. H. Baksht, V. F. Tarasenko, A. V. Fedunin, S. A. Chaikovskiy, P. N. Aruev, V. V. Zabrodskii, M. V. Petrenko, N. A. Sobolev, and V. L. Suhanov, *Instrum. Exp. Tech.* **58**, 102 (2015). <https://doi.org/10.1134/S0020441215010017>
  36. V. V. Zabrodskii, V. P. Belik, P. N. Aruev, B. Ya. Ber, S. V. Bobashev, M. V. Petrenko, and V. L. Sukhanov, *Tech. Phys. Lett.* **38**, 812 (2012). <https://doi.org/10.1134/S1063785012090143>

37. V. A. Tokarev, V. K. Gusev, N. A. Khromov, M. I. Patrov, Yu. V. Petrov, and V. I. Varfalomeev, *J. Phys.: Conf. Ser.* **1094**, 012003 (2018).  
<https://doi.org/10.1088/1742-6596/1094/1/012003>
38. A. V. Voronin, V. Yu. Goryainov, A. A. Kapralov, V. A. Tokarev, and G. Yu. Sotnikova, *Tech. Phys.* **68** (5), 580 (2023).  
<https://doi.org/10.21883/TP.2023.05.56063.262-22>
39. N. A. Khromov, E. O. Vekshina, V. K. Gusev, N. V. Litunovskii, M. I. Patrov, Yu. V. Petrov, and N. V. Sakharov, *Tech. Phys.* **66**, 409 (2021).  
<https://doi.org/10.1134/S1063784221030117>
40. A. V. Voronin, V. Yu. Goryainov, V. V. Zabrodskii, E. V. Sherstnev, V. A. Kornev, P. N. Aruev, G. S. Kurskiev, N. A. Zhubr, and A. S. Tukachinskii, *Tech. Phys.* **67** (15), 2377 (2022).  
<https://doi.org/10.21883/TP.2022.15.55263.188-21>
41. E. E. Tkachenko, G. S. Kurskiev, N. S. Zhil'tsov, A. V. Voronin, V. Yu. Goryainov, E. E. Mukhin, S. Yu. Tolstyakov, V. I. Varfolomeev, V. K. Gusev, V. B. Minaev, A. N. Novokhatskii, M. I. Patrov, Yu. V. Petrov, N. V. Sakharov, E. O. Kiselev, et al., *Vopr. At. Nauki Tekh., Ser.: Termoyad. Sint.* **44** (3), 52 (2021).  
<https://doi.org/10.21517/0202-3822-2021-44-3-52-62>
42. V. V. Bulanin, G. S. Kurskiev, V. V. Solokha, A. Yu. Yashin, and N. S. Zhiltsov, *Plasma Phys. Control. Fusion* **63**, 122001 (2021).  
<https://doi.org/10.1088/1361-6587/ac36a4>

*Translated by L. Mosina*

**Publisher's Note.** Pleiades Publishing remains neutral with regard to jurisdictional claims in published maps and institutional affiliations.